Properties of atomic layer deposited iron oxide and bismuth oxide chloride structures

Helina Seemen*[a], Kaupo Kukli[a], Taivo Jõgiaas[a], Peeter Ritslaid[a], Joosep Link[b], Raivo Stern[b], Salvador Dueñas[c], Helena Castán[c] and Aile Tamm[a]

Address:

[a]Institute of Physics, University of Tartu, W. Ostwaldi 1, 50411 Tartu, Estonia,

[b]National Institute of Chemical Physics and Biophysics, Akadeemia tee 23, 12618 Tallinn, Estonia,

[c]Department of Electronics, University of Valladolid, Paseo Belén, 15, 47011 Valladolid, Spain

Email: Helina Seemen – helina.seemen@ut.ee

* Corresponding author

Abstract

Two-component crystalline thin film structures consisting of continuous ε-Fe$_2$O$_3$ bottom layers followed by top layers of BiOCl nanoflakes were grown using atomic layer deposition from FeCl$_3$ and BiCl$_3$ at 375 °C. Si(100) planar wafer, three-dimensional Si structures and conductive TiN/Si were exploited as substrates. Electrical measurements revealed that the deposited structures were moderately leaky, as the structures showed rectifying behavior affected by visible illumination. Magnetization in these films in the as-deposited state was nonlinear, saturative, and exhibited well-defined coercive fields. Annealing changed the surface morphology, phase composition and reduced the magnetic behavior of the thin films.

Keywords

Atomic layer deposition, ε-Fe$_2$O$_3$, BiOCl nanoflakes, visible illumination, thin films

Nanostructured materials, vapor deposition, magnetization, magnetic measurements, scanning electron microscopy (SEM), X-ray diffraction

1. Introduction

Fe_2O_3 and BiOCl nanocomposites are of interest in the development of thin light-sensitive magnetic nanomaterials [1-3]. The ε-Fe_2O_3 has caught the attention, inter alia, due to its room-temperature multiferroic properties including high coercivity [4-7] and the point group symmetry of ε-Fe_2O_3 structure, which allows the occurrence of physical effects such as pyroelectricity, piezoelectricity, optical activity, or second-harmonic generation [8,9].

At the same time, BiOCl is known as wide bandgap semiconductor material [10-12] that has high chemical stability [13], good photostability [10], excellent photocatalytic activity [11-14], indirect optical transition property [12], and high photocorrosion stability in the presence of redox pairs [10]. Doping BiOCl with different metals, ions and rare-earth ions can enhance its properties and further broaden the area of applications [15, 16]. For example, doping BiOCl with Co [17] or Fe [18] enhances photocatalytic activity [15]; and doping BiOCl with magnetic ions (for example Fe, Ni, Co) and rare-earth ions can introduce ferromagnetic properties [15].

Out of studies on iron oxide-BiOCl composites in general, BiOCl/α-Fe_2O_3 composite synthesized using hydrothermal and solution combustion method has been reported, and enhanced photocatalytic activity noticed [19]. Another study was dedicated on Fe_3O_4/BiOCl nanocomposite, and it was stated to be an effective photocatalyst to degrade the organic dyes [20]. In another study, BiOCl/α-Fe_2O_3 heterojunction nanoplates, synthesized through an in-situ oxidation, demonstrated enhanced visible-light-driven photocatalytic performance for degrading organic pollutants and reducing Cr(VI) [21]. In yet another study aimed at the enhancement of photocatalytic performance, α-Fe_2O_3/BiOCl heterojunctions were synthesized by growing and assembling α-Fe_2O_3 nanoplates to BiOCl microflowers via a two-step route [22]. In addition, α-Fe_2O_3/BiOCl composites, in which uniform Fe_2O_3 nanocubes have been deposited on the BiOCl nanosheets via a facile hydrothermal process, were also studied due to their enhanced photocatalytic activity [23]. Furthermore, α-Fe_2O_3/BiOCl p/n heterojunctions were prepared via *in situ* hydrolysis method and improved photodegradation properties for mixture dyes were noticed [24].

Even though there are several studies published on α-Fe_2O_3/BiOCl or Fe_3O_4/BiOCl composites, to our knowledge, the properties of ε-Fe_2O_3-BiOCl composites have not been published before. Combining these two materials with, e.g., attractive magnetic and electrical properties into one nanocomposite can possibly enhance the properties of the material and combine the advantages of both materials into one composite. This can possibly be an attractive combination, e.g., in search for photosensitive magnetic nanomaterials [1-3] and light absorber materials.

The ε-Fe_2O_3 phase has, besides atomic layer deposition (ALD) [4], been grown using different chemical and physical techniques, e.g., pulsed laser deposition [6, 25], electrodeposition [26], sol-gel synthesis [27-29], plasma-enhanced chemical vapor deposition [30] and two-step CVD/sputtering approach [31]. In a study published by Tanskanen *et al.* at 2017, the growth of ε-Fe_2O_3 thin films with ALD was presented for the first time [4]. Some of the several advantages of ALD method compared to other methods are precise thickness control over large substrate areas and conformity over complex surface architectures [4, 32, 33].

BiOCl has been synthesized using, e.g., sol-gel route [15], facile solvothermal [34,35] and hydrolysis [36] route, alcoholysis-coating method [11], aerosol-assisted chemical vapor deposition [37], thermal evaporation [13], wet chemical route [14,38], facile low-temperature vapor-phase synthesis route [10] and atomic layer deposition [39,40]. The amount of published studies that reflect on atomic layer deposited BiOCl has so far been quite scarce. In the case of those sited studies the focus of the study has been elsewhere, but in regards with BiOCl, it has been briefly mentioned that using bismuth chloride as one of the precursors resulted in BiOCl formation [39]. In addition, in the deposition temperature range of 300 – 400 °C, the films consisted of the BiOCl phase while an increment of the temperature to 500 °C resulted in bismuth oxychlorides with a lower chloride content, *i.e.* $Bi_{24}O_{31}Cl_{10}$ [40]. To our knowledge, the ε-Fe_2O_3-BiOCl composites have not been deposited via ALD before.

In the present study, we report composites consisting of a ε-Fe_2O_3 layer at the bottom and BiOCl nanoflakes on the top, grown using an ALD method. $FeCl_3$ and $BiCl_3$ were used as the metal precursors and H_2O was used as the oxygen precursor in the ALD process. Thickness, structure, morphology, magnetic and electrical behavior of the samples and, complementarily, cross-sections of the selected films deposited on three-dimensional (3D) substrates were examined. Selected

samples were also annealed to determine the effect of heat-treatment on the film morphology, crystal structure, and magnetic properties.

2. Experimental

The films were grown in a flow-type in-house built hot-wall ALD reactor [41] from $FeCl_3$ (99.99 %, Sigma Aldrich) and $BiCl_3$ (99.999 % PURATREM) as the metal precursors and H_2O as the oxygen precursor. N_2 (99.999 %, AGA) was used as the carrier and purge gas. Deposition temperature of 375 °C was selected for bismuth-containing constituents in two-component samples based on preliminary experiments (see the Supplementary Material). A BiOCl film deposited using the cycle sequence of $500 \times (BiCl_3 + H_2O)$ (Table I) at 300 ± 2 °C was defined as a reference sample. The $BiCl_3$ evaporation temperature for that sample was 126 ± 2 °C. For the rest of the samples, $FeCl_3$ and $BiCl_3$ were evaporated at 135 ± 2 °C and 164 ± 2 °C, respectively, from open boats inside the reactor, and transported to the substrates by the carrier gas flow. During the deposition, the chamber pressure remained in the range of 220-232 Pa. The precursor pulse durations and purge lengths for both oxides were 5-2-2-5 s, denoting the sequence of metal precursor pulse – N_2 purge – H_2O pulse – N_2 purge. Pieces of undoped Si(100) wafers, three-dimensional (3D) structures and highly-doped Si covered by TiN layer were exploited as substrates. TiN layer was deposited using $TiCl_4/NH_3$ process on an ASM A412 Large Batch 300 mm reactor at Fraunhofer IPMS-CNT. The conducting substrates were based on (100)-oriented silicon with resistivity in the range of $0.014 – 0.020$ $\Omega \cdot cm$, i.e., boron-doped to concentrations up to $5 \times 10^{18} – 1 \times 10^{19}/cm^3$, and coated with 10 nm thick chemical vapor deposited titanium nitride layer. The same growth experiments were conducted on all substrates, including the 3D stacks, simultaneously without changing cycle time parameters or amounts of cycles, in order to examine whether the cycle times ensuring reasonably short growth processes, film thickness providing sufficient amounts of magnetic material, and growth conformal with substrates of challenging topology could be at least partially combined. Selected samples were also annealed in the air environment at 800 °C for 30 minutes to determine the effect of heat-treatment on magnetic and structural properties.

The mass thickness and elemental composition of the films were measured by wavelength-dispersive X-ray fluorescence (WDXRF) spectrometer Rigaku ZSX 400 with the ZSX software.

The X-ray tube used in spectrometer ZSX 400 is the end window type. The standard target element is Rh (Rh-KA excitation energy is 23.2 KeV). The X-ray emission was gathered from the area with the diameter of 10 mm. The elemental composition and film thickness were calculated using SQX method, and selected samples were comparatively analyzed by means of FP Quant. The former method ignores layered structures of solid films, considering the layers as homogeneous mixtures. In the latter case, the substrate is defined at first and separately, followed by distinct component layers in the order of their deposition sequence.

The crystal structure was evaluated by grazing incidence X-ray diffractometry (GIXRD), using a X-ray diffractometer SmartLab Rigaku with incidence angle of 1 deg and CuKα radiation, which corresponds to an X-ray wavelength of 0,15406 nm. The morphology of deposited structures on Si substrate and the cross-sections of the films on 3D-substrates were investigated by scanning electron microscopy (SEM) using FEI Helios Nanolab 600 DualBeam microscope. The electron probe microanalysis were performed using an energy-dispersive X-ray (EDX) spectrometer INCA Energy 350 (Oxford Instruments), attached to the same SEM.

Selected films were subjected to magnetic measurements. The measurements were performed using the P525 Vibrating Sample Magnetometer (VSM) option of the Physical Property Measurement System (PPMS) 14T (Quantum Design). Rectangular samples were fixed with GE 7031 vanish to the commercial quartz sample holders (Quantum Design). Hysteresis measurements were carried out at room temperature (300 K) by scanning the magnetic fields from -40000 to +40000 Oe (from -3183.098 to 3183.098 kA/m) parallel to the film surface. The diamagnetic signal arising from the silicon substrate was subtracted from the general magnetization curve for all the samples in which the ferromagnetic-like response was detected. To gain magnetization in the units of emu/cm^3, the measured magnetic moment was divided with volume, estimated from the film thickness calculated from the XRF measurements and the measured surface area of the sample.

In order to carry out the electrical measurements, metal-insulator-metal (MIM) structures were prepared on conducting substrates. Top electrodes with area of 0.204 mm^2 were formed by electron beam evaporation of 120-150 nm thick Al layers directly contacting Fe_2O_3-BiOCl composites through a shadow mask. Capacitance-voltage (C–V) and current-voltage (I–V) measurements were carried out in a light-proof and electrically shielded box. Samples were

electrically characterized in both DC and AC regimes using a Keithley 4200SCS semiconductor analyzer.

3. Results and Discussion

3.1 Film growth, formation, structure and morphology

Fe_2O_3 reference film grew to the thickness of 46 ± 1 nm after 250 growth cycles on planar silicon substrate. The growth rate of Fe_2O_3 was, thus, ~0.18 nm/cycle. In the case of the composites, the thicknesses of the Fe_2O_3 layers were evaluated to be in the range of ~0.8 nm to ~36 nm (Table I). One could see that the estimated actual growth rates for iron oxide layers tended to decrease with the number of the Fe_2O_3 deposition cycles. This could be expected, considering that, at the beginning of the ALD growth, the dependence of the film thickness on the number of cycles most often remains sublinear and growth rate somewhat retarded, due to the nucleation issues at the early stages of the growth. Although, some fluctuations and experimental uncertainties occurred inevitably. In an earlier study on ALD of Fe_2O_3 from $FeCl_3$ and H_2O, the average growth rate of the films was ~0.07 nm/cycle at 360 ℃, measured for films grown in a flow-type commercial research-scale ALD-reactor [4].

The thickness of the BiOCl reference sample was 7.8 ± 1.0 nm and the average growth rate evaluated as 0.03 nm/cycle. The thickness calculations were made assuming that the oxide layers were uniform in thickness; possible thickness non-uniformity of the layers along and across the gas flow directions on the substrates, and the possible influence of morphological features on growth rate, were not taken into account in this calculation. In the case of the composites in the present study, the estimated thicknesses were in the range of ~0.7 nm to ~27 nm and the growth rates remained between ~0.003 and 0.08 nm/cycle (Table I).

The low growth rates of both the BiOCl reference film and the thinnest composite resulted in low thicknesses of the samples because often the overall growth rate does not exactly correspond to the growth rate during the first few nanometers. This phenomenon is also known as the incubation or retardation period during the initiation of the ALD [42-44]. In addition, the substrate material may influence the growth rates of some materials, that is, the metal oxide (or in this case metal

6

oxide chloride) can sometimes grow to the top of the substrate material with different rate compared to the top of another oxide layer.

The influence of the substrate material was noticed at the early stages of the experiments, when the growth of BiOCl on SiO_2/Si substrate occurred ineffective. In the case of repetitive depositions and the observations made at different stages of the deposition series (both before and after the successful depositions of composites), it was noticed that BiOCl hardly grew on the surface of SiO_2/Si(100) substrate after 250 cycles applied at 375 °C, as during the XRF measurements Bi (signal) remained below the reliability limit or, in some cases, also below detection limit. On the other hand, it was noticed that under the same conditions (250 ALD cycles at 375 °C) BiOCl grew reliably on the top of the 22 nm thick Fe_2O_3 layer as the estimated BiOCl layer thickness in the latter case was as high as 16 nm (Table I).

As results of the annealing in the air environment at 800 °C for 30 minutes, the Fe_2O_3 layer thicknesses decreased by a few nanometers (Table II). In addition, annealing noticeably reduced the amount of chlorine in the samples as, after annealing, either the Cl signal decreased below the reliability limit, or chlorine was not detected at all during the XRF measurements (see the Supplementary Material). The lack of chlorine indicates that, after annealing, bismuth-containing component was no longer present in the form of bismuth oxychloride, but probably in some phase of bismuth oxide instead.

Table I: Estimated thicknesses and the deposition rates of the reference thin films and Fe_2O_3-BiOCl composites deposited on Si substrate. The estimated thicknesses were calculated from elemental composition measured with XRF and using the densities of 5.15 g/cm³ and 7.36 g/cm^3 for Fe_2O_3 and BiOCl, respectively. The calculations were made assuming that the oxide and oxide chloride layers were uniform in thicknesses.

	ALD growth cycle sequence	Thickness of Fe_2O_3, nm	Thickness of BiOCl, nm	Growth rate of Fe_2O_3, nm/cycle	Growth rate of BiOCl, nm/cycle
a)	$250 \times Fe_2O_3$ (Fe_2O_3 ref.)	46 ± 1	-	0.18	-
b)	$175 \times Fe_2O_3 + 280 \times BiOCl$	31 ± 1	19 ± 1	0.18	0.067
c)	$250 \times Fe_2O_3 + 315 \times BiOCl$	36 ± 1	27 ± 1	0.14	0.08
d)	$80 \times Fe_2O_3 + 280 \times BiOCl$	13 ± 1	20 ± 1	0.16	0.07

e)	$90 \times Fe_2O_3 + 280 \times BiOCl$	13 ± 1	15 ± 1	0.15	0.05
f)	$250 \times Fe_2O_3 + 250 \times BiOCl$	22 ± 1	16 ± 1	0.09	0.065
g)	$105 \times Fe_2O_3 + 230 \times BiOCl$	9 ± 1	11 ± 1	0.08	0.05
h)	$20 \times Fe_2O_3 + 250 \times BiOCl$	0.8 ± 0.5	0.7 ± 0.5	0.04	0.003
i)	$500 \times BiOCl$ (BiOCl ref.)	-	8 ± 1	-	0.03

Table II: Estimated thickness of the reference thin films and Fe_2O_3-Bi_2O_3 structures deposited on Si substrate after annealing according to the XRF measurements. The thickness was calculated using the densities of 5.15 g/cm³ and 8.55 g/cm³ for Fe_2O_3 and Bi_2O_3, respectively.

	ALD growth cycle sequence	Fe_2O_3 thickness, nm	Bi_2O_3 thickness, nm
a)	$250 \times Fe_2O_3$ (Fe_2O_3 ref.)	40 ± 1	-
b)	$175 \times Fe_2O_3 + 280 \times BiOCl$	28 ± 1	9 ± 1
d)	$80 \times Fe_2O_3 + 280 \times BiOCl$	11 ± 1	7 ± 1
f)	$250 \times Fe_2O_3 + 250 \times BiOCl$	12 ± 1	6 ± 1
g)	$105 \times Fe_2O_3 + 230 \times BiOCl$	6 ± 1	3 ± 1
h)	$20 \times Fe_2O_3 + 250 \times BiOCl$	0.3 ± 0.5	-
i)	$500 \times BiOCl$ (BiOCl ref.)	-	5 ± 1

It is noteworthy that application of the two different XRF calculation methods, SQX and FP Quant, have resulted in comparable compositions in terms of iron to bismuth ratios. Thus, for the film grown using the cycle sequences of $175 \times Fe_2O_3 + 280 \times BiOCl$ and, the Fe/Bi ratios were 1.02 and 1.03, when calculated by SQX and FP Quant, respectively. For the film grown using the cycle sequence of $250 \times Fe_2O_3 + 250 \times BiOCl$, the Fe/Bi ratio turned out to be 0.81 in both cases.

GIXRD patterns (Figure 1) confirmed that all the reference thin films and Fe_2O_3-BiOCl composites, except for the film grown using 20 Fe_2O_3 cycles followed by 250 cycles of BiOCl, were crystallized already in the as-deposited state. The latter film was not crystallized probably due to its very small thickness. The diffractogram of the reference Fe_2O_3 thin film (Figure 1, a) contained reflections attributable to the orthorhombic ε-Fe_2O_3 phase (ICSD 173024), and it did not demonstrate any preferred orientation. Out of the five iron(III) oxide polymorphs, this rare, synthetic and metastable ε-Fe_2O_3 phase has been found and synthesized only in nanoscale samples, including specimens in a thin film form [4, 6, 25-27]. It has been a phase of interest due to its

room-temperature multiferroic properties including high coercivity [4-7], as a large coercive field of 20 kOe has been measured for ε-Fe_2O_3 at room temperature, which is the largest among metal oxide based magnetic materials [5, 7, 45]. The explanation behind achieving such large coercive field was the large magneto-crystalline anisotropy of ε-Fe_2O_3 and the formation of just a single magnetic domain in suitably sized nanocrystals [7]. In an ALD study by Tanskanen *et al.* [4] the ε-Fe_2O_3 phase was present in a lower deposition temperature range (280-320 °C), and at 340 °C the phase had changed to hematite.

The diffractogram of the reference BiOCl thin film (Figure 1, i) had one strong reflection that was narrow and intense enough to conclude that the crystallization had taken place. This strong reflection, indexed as 104, at 55.1° could be attributed to tetragonal BiOCl (PDF card 00-006-0249). Due to the similar location for cubic reflection of 532 at 55.0° and monoclinic reflection of 014 at 55.1°, Bi_2O_3 could not be completely ruled out at this point. The small thickness of the reference film might be the main reason for the appearance of only one peak.

In the case of the composites (Figure 1), especially in the case of the film grown using the cycle sequence of $175 \times Fe_2O_3 + 280 \times BiOCl$ (Figure 1, b) the dominant phase was tetragonal BiOCl, as there appeared twelve reflections attributable to the tetragonal BiOCl (PDF card 00-006-0249) on the diffractogram. In an earlier study by Schuisky *et al.* [40], the formation of BiOCl from the same precursors at the deposition temperature range of 300-400 °C has been observed. In the case of the other composites in the present study, the amount of clear reflections was smaller compared to the $175 \times Fe_2O_3 + 280 \times BiOCl$ structure and the peak intensities varied noticeably, but the dominant phase was the same tetragonal BiOCl. It also appeared that the orthorhombic ε-Fe_2O_3 phase was present in the other deposited composites, although the peak intensities varied noticeably.
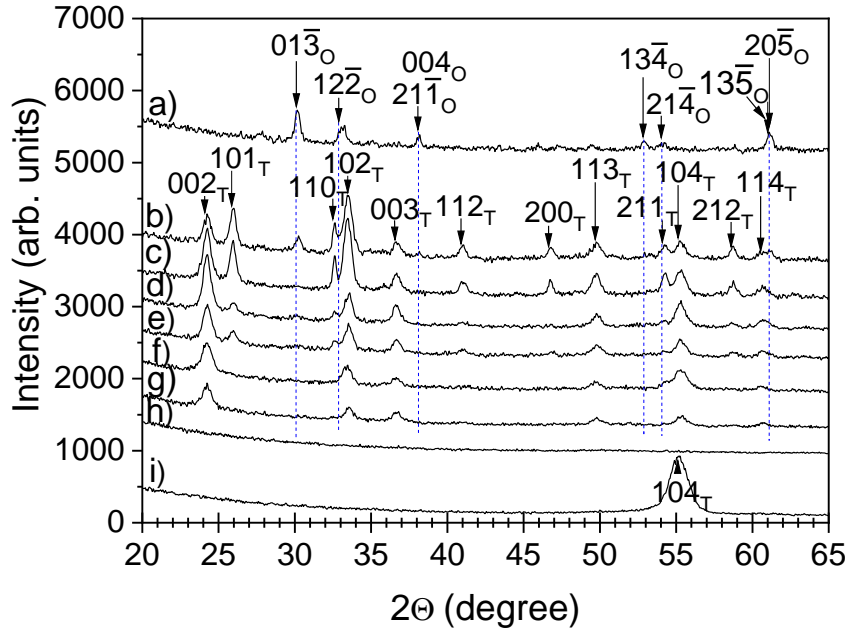
Figure 1: X-ray diffraction patterns from the Fe_2O_3 and BiOCl reference thin film and Fe_2O_3-BiOCl structures, in the as-deposited state. Miller indexes assigned after crystallization are indicated with "T" for tetragonal BiOCl (PDF card 00-006-0249) and "O" for orthorhombic ε-Fe_2O_3 phase (ICSD 173024). See Table I as the reference for the growth cycle sequences behind these diffractogram labels.

The XRD measurements on annealed samples (Figure 2), revealed some clear changes in the phase composition. The diffractogram of the reference Fe_2O_3 thin film (Figure 2, a) after annealing contained ten distinct reflections attributable to the rhombohedral α-Fe_2O_3 phase (PDF card 04-003-2900), also known as hematite. This result was expected, as the transformation of metastable ε-Fe_2O_3 to stable α-Fe_2O_3 has been reported before [4, 27, 46]. As mentioned above, this ε-Fe_2O_3 has been observed as an intermediate phase between γ-Fe_2O_3 (maghemite) and α-Fe_2O_3 (hematite) upon heating [46, 47]. The desired outcome of the annealing would have been a phase change and the formation of bismuth ferrite containing interface between the two layers. The preliminary annealing experiments made of the selected samples at 600 °C for 30 minutes showed that compared to the same type of samples in the as-deposited state, the XRD peak heights had generally decreased, with some exceptions, and no clear phase change had not yet taken place (See the Supplementary material). Therefore, the temperature of 800 °C was selected for annealing.

10

The diffractogram of the reference BiOCl film grown using 500 ALD cycles (Figure 2, i) revealed that the phase had changed, after annealing, from BiOCl to cubic (PDF card 00-045-1344) and monoclinic Bi_2O_3 (PDF card 00-041-1449) polymorphs. This was somewhat expected because the annealing can well reduce the amount of Cl contributing to the composition. In the case of the composites, the same monoclinic and cubic Bi_2O_3 phases were present as dominant phases after annealing, and rhombohedral α-Fe_2O_3 phase was present to some extent. While comparing the diffractograms of the composites, one could notice that the peak intensities vary. In the case of the sample grown using cycle sequence of $175 \times Fe_2O_3 + 280 \times BiOCl$ the peak intensities (especially the peaks connected with α-Fe_2O_3 phase) were noticeably higher and therefore the latter layers must have been structurally more ordered compared to the other composites.
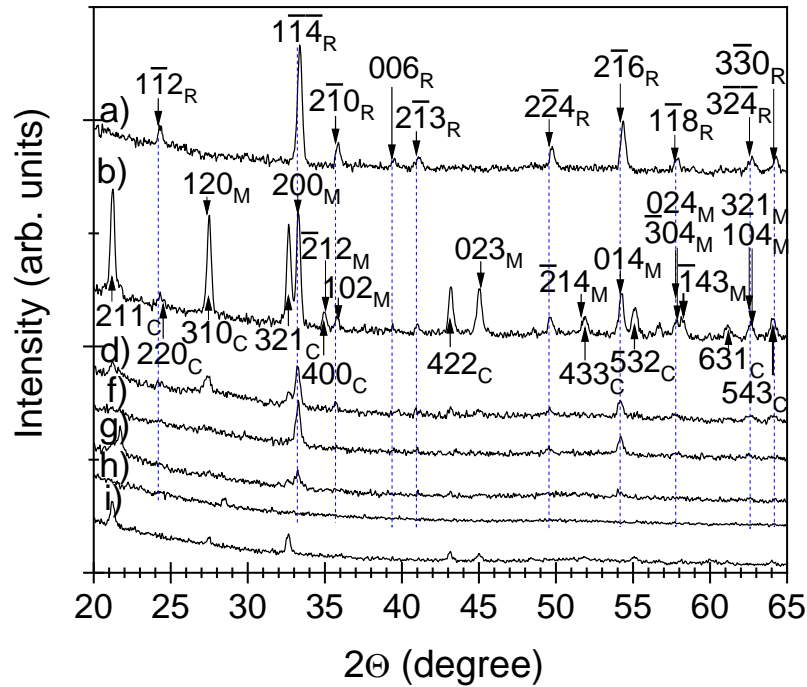
Figure 2: X-ray diffraction patterns from the reference Fe_2O_3 and BiOCl thin films and selected Fe_2O_3-BiOCl structures after annealing at 800 °C for 30 min. Miller indexes assigned after crystallization are indicated with "R" for rhombohedral Fe_2O_3, which is also known as hematite (PDF card 04-003-2900), "M" for monoclinic Bi_2O_3 (PDF card 00-041-1449) and "C" for cubic Bi_2O_3 (PDF card 00-045-1344), as labels. For the growth cycle sequences behind the diffractograms, see the Table II.

11

Scanning electron microscopy revealed that in the case of the reference Fe_2O_3 film (Figure 3.a) the surface was uniformly covered by grain-like features characteristic of crystallized thin film and ε-Fe_2O_3 phase. As similar-looking, multi-faced crystals were seen in an earlier study on atomic layer deposited ε-Fe_2O_3 [4], where the maximum size of the grains was 120 nm, which is noticeably larger than in the case of our Fe_2O_3 reference film that had the maximum size of grains ca. 70 nm. The difference in grain size was caused by the differences in the thicknesses of the films, as the ε-Fe_2O_3 film in the earlier study [4] was ~260 nm thick, whereas the maximum thickness in our samples was ~46 nm.

In the case of the reference BiOCl film grown after 500 deposition cycles (Figure 3.b) the surface became quite uniformly covered with a continuous solid material and a few flake-like features started to appear. In the case of the thinnest composite grown using the cycle sequence of 20 × Fe_2O_3 + 250 × BiOCl (Figure 3.c) small grain-like features were present. As the thicknesses were low (0.8 nm Fe_2O_3 + 0.7 nm BiOCl), part of the visible grain structures originated, possibly, from the iron oxide layer nucleating after 20 ALD cycles of Fe_2O_3.

In the case of the other deposited structures (Figure 3.d-i), nano-flake and grain-like features started to form, with their appearance depending on the amount of cycles applied to grow the constituent layers. Grain-like features seen on composites are related with Fe_2O_3 as they resemble the morphology of the reference Fe_2O_3 film, and the average size of these grain-like features was related to the thickness of the Fe_2O_3. Meaning that in the samples containing thinner Fe_2O_3 layer (e.g., Figure 3.i), smaller grains were formed compared to the samples with thicker Fe_2O_3 layer (see Supplementary Material).

The nano-flake-like features seen in the case of 6 two-layer structures (Figure 3.d-i) are related to bismuth oxychloride. There are several other studies published, where in the case of BiOCl similar flake-like features were observed [10, 14, 19, 22-24, 35-38, 48]. In these studies, BiOCl has been synthesized via different routes and on different substrate materials. One can refer to, spherical Fe_3O_4@C@BiOCl nanocomposites [48] and flower-like BiOCl [35] synthesized by solvothermal process, different BiOCl nanostructures synthesized using low-temperature chemical vapor transport [10], BiOCl synthesized by wet chemical route [14, 36, 38] and aerosol-assisted chemical vapour deposition [37], and Fe_2O_3/BiOCl p/n heterojunctions synthesized by in situ hydrolysis

method [24]. Despite the different methods used to create BiOCl in different shapes listed above, similarities in the morphology are very clearly visible.
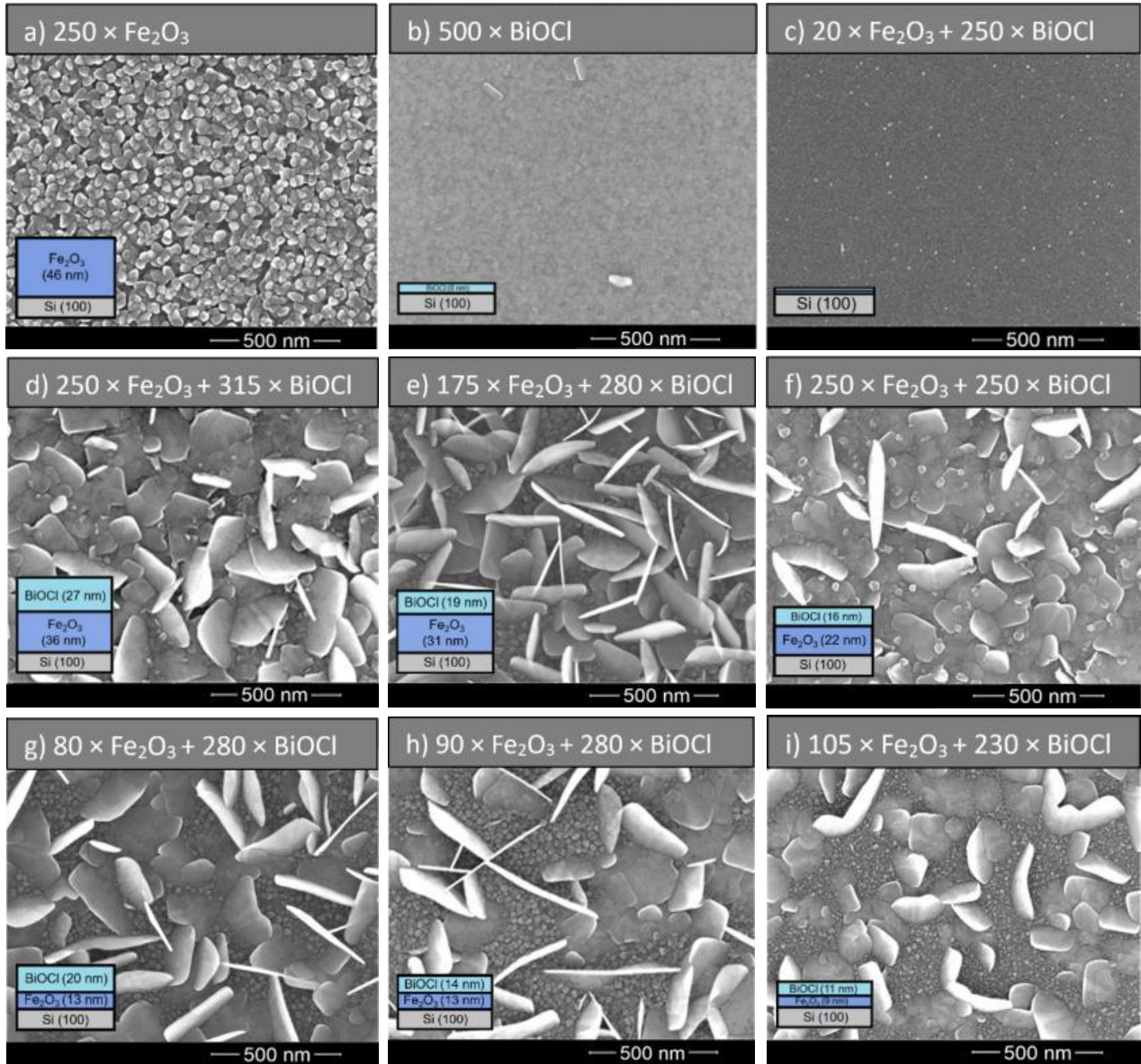
Figure 3: The bird-eye view of the SEM images of the reference objects and Fe_2O_3-BiOCl structures in the as-deposited state. Illustrative schematics show the calculated thicknesses of the layers listed in Table I. Growth cycle sequences are given by labels.

According to the morphology seen in the SEM images (Figure 3), one could propose that the bismuth oxychloride nanoflakes could not uniformly cover the Fe_2O_3 layer. The cross-sections of the reference Fe_2O_3 film (Figure 4.a) and the composite grown using the cycle sequence of $175 \times$

$Fe_2O_3 + 280 \times BiOCl$ (Figure 4.b) were investigated to evaluate this proposal. In both cases, the Fe_2O_3 layer was uniformly deposited and the thicknesses of the Fe_2O_3 layers measured from SEM cross-section images matched with the thicknesses calculated from the XRF results (Table I). Cross-sections of the samples additionally confirmed that the upper BiOCl nanoflakes did not cover the Fe_2O_3 layer uniformly as one can decide on the basis of nanoflakes standing at different angles with grains from the Fe_2O_3 layer present between and below the flakes (Figure 4.b). The thicknesses of 10 randomly selected nanoflakes ranged from 8 to 29 nm (3 of these are displayed in Figure 4.b).
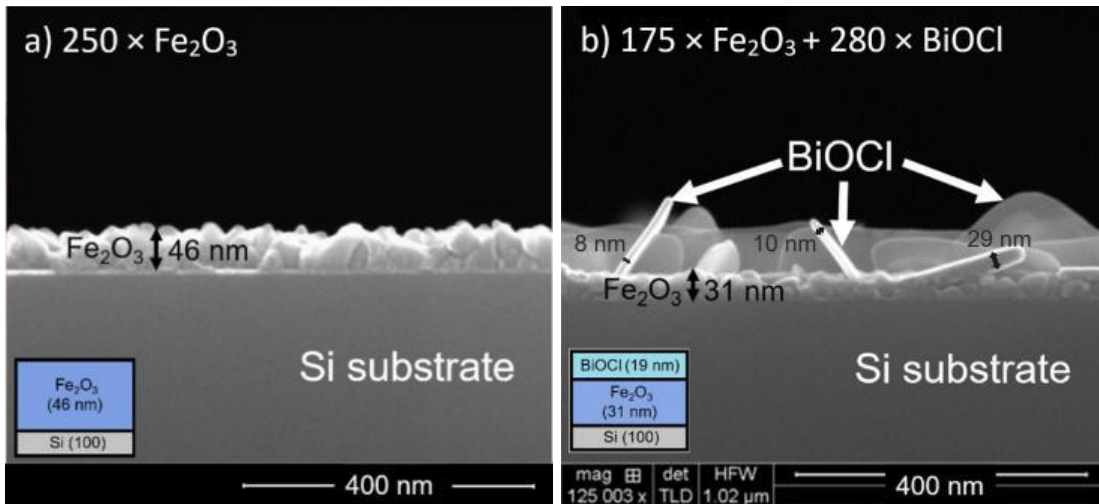

Figure 4: Cross-sectional SEM images of a) the reference Fe_2O_3 film and b) composite deposited using the cycle sequences $175 \times Fe_2O_3 + 280 \times BiOCl$. Dark arrows indicate the thicknesses measured from the SEM images.

While characterizing the films grown on 3D substrates, the bird-eye view SEM images showed, in the case of the reference Fe_2O_3 film (Figure 5.b), a regular pattern of the openings to the trenches located similarly to those in the uncovered 3D sample with empty trenches (Figure 5.a). This means that during the ALD process, the thin film has followed the shape of the 3D structure substrate, as expected for the ALD process, and closing of the openings to the trenches was avoided. In the case of the film grown using the cycle sequence of $175 \times Fe_2O_3 + 280 \times BiOCl$

(Figure 5.c) fewer trenches appear to be remained open compared to the reference Fe_2O_3 film on the 3D substrate.
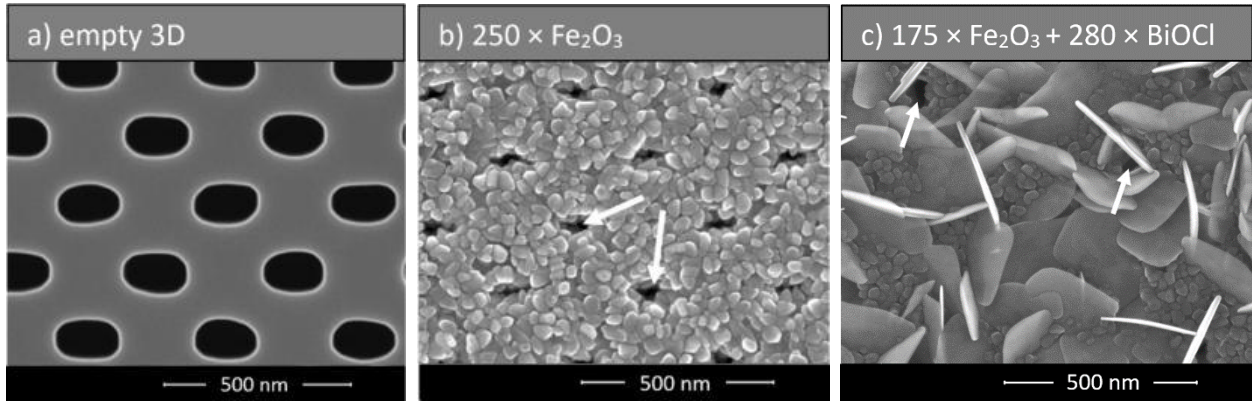
Figure 5: The bird-eye view SEM images of the a) empty 3D substrate, b) Fe_2O_3 reference thin film, and c) sample grown using the cycle sequence of $175 \times Fe_2O_3 + 280 \times BiOCl$ on 3D substrate. The tips of the white arrows point to some of the holes.

The cross-section of the Fe_2O_3 reference 3D sample (Figure 6) confirmed that the Fe_2O_3 thin film was almost uniformly deposited also to the inner walls of the 3D structure. The thickness of the layer decreased noticeably towards the bottom of the trench, though, indicating that the step coverage could not reach 100 %. The cross-section of the sample grown using the cycle sequence of $175 \times Fe_2O_3 + 280 \times BiOCl$ on 3D substrate (Figure 7) showed, interestingly, that some BiOCl flakes were formed deep inside the trenches in addition to the grains of the Fe_2O_3. The majority of nanoflakes were, expectedly, deposited and formed at the wafer level on top of the trench (Figure 7.a), but some nano-flakes could also be found at the middle (Figure 6.b) and bottom (Figure 7.c) parts of the 3D trench along with its ~6 μm depth.
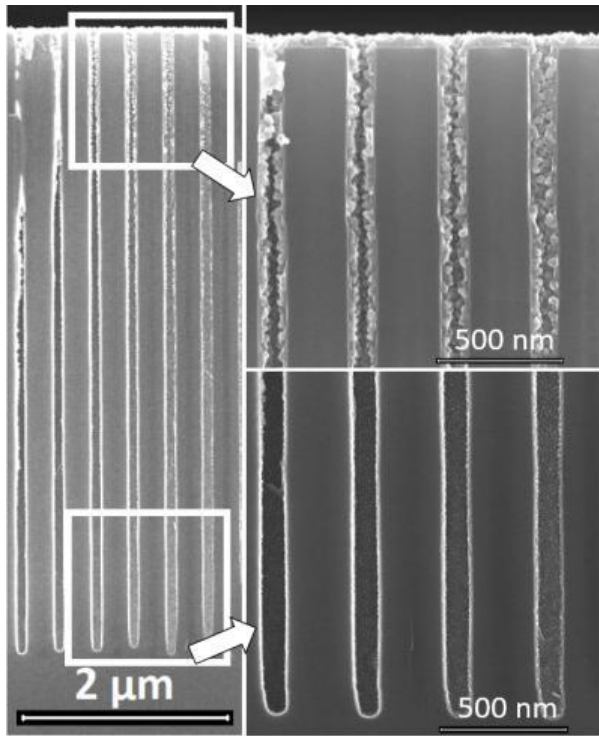
Figure 6: SEM image of the cross-section of the reference Fe_2O_3 film deposited on 3D substrate. White boxes and arrows indicate that the upper right image was taken from the top and bottom image from the bottom part of the trenched structure.
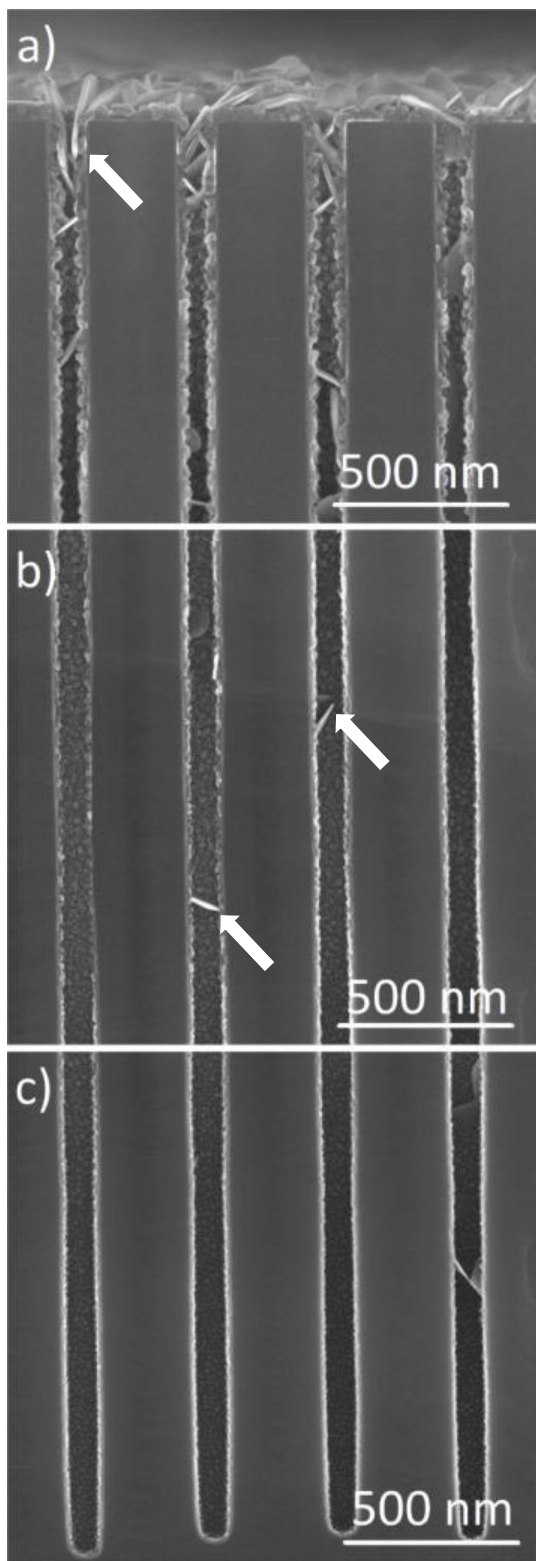
Figure 7: SEM images of the cross-section of the a) upper, b) middle and c) bottom part of the $175 \times Fe_2O_3 + 280 \times$ BiOCl on 3D substrate. White arrows point to selected BiOCl flakes.

According to the SEM, annealing at 800 °C for 30 minutes had noticeably changed the morphology of all the selected samples (Figure 8, 9). The reference Fe_2O_3 film (Figure 8.a) became uniformly covered with a pattern of grains with rounded edges that visually appeared to be not as distinct, sharp and separated as those in the as-deposited state. In the case of the BiOCl reference film grown using 500 cycles (Figure 8.b) and four two-component structures (Figure 9 and Figure S. 4 in Supplementary Material), the flake-like features disappeared after annealing and were replaced by alternating lighter and darker areas.
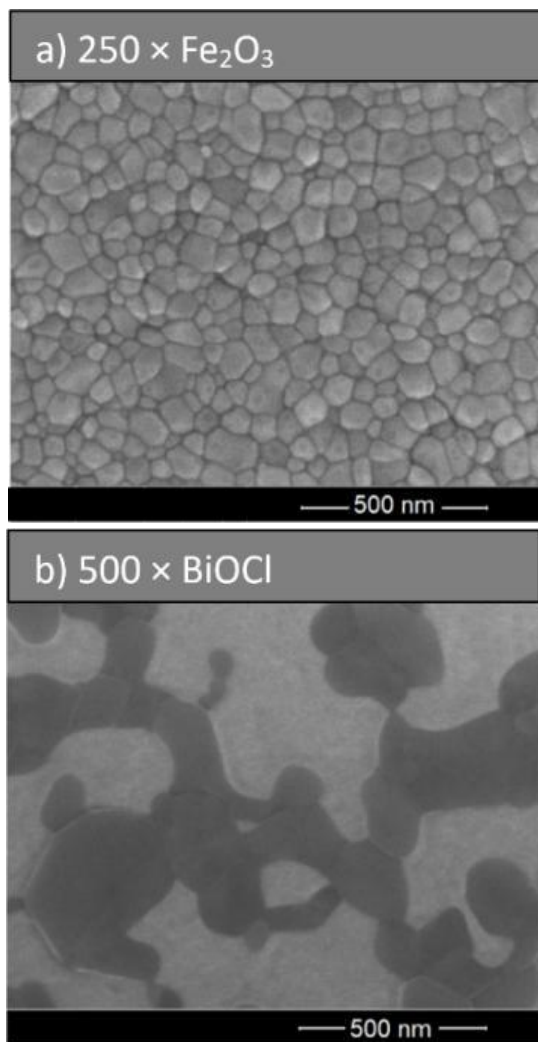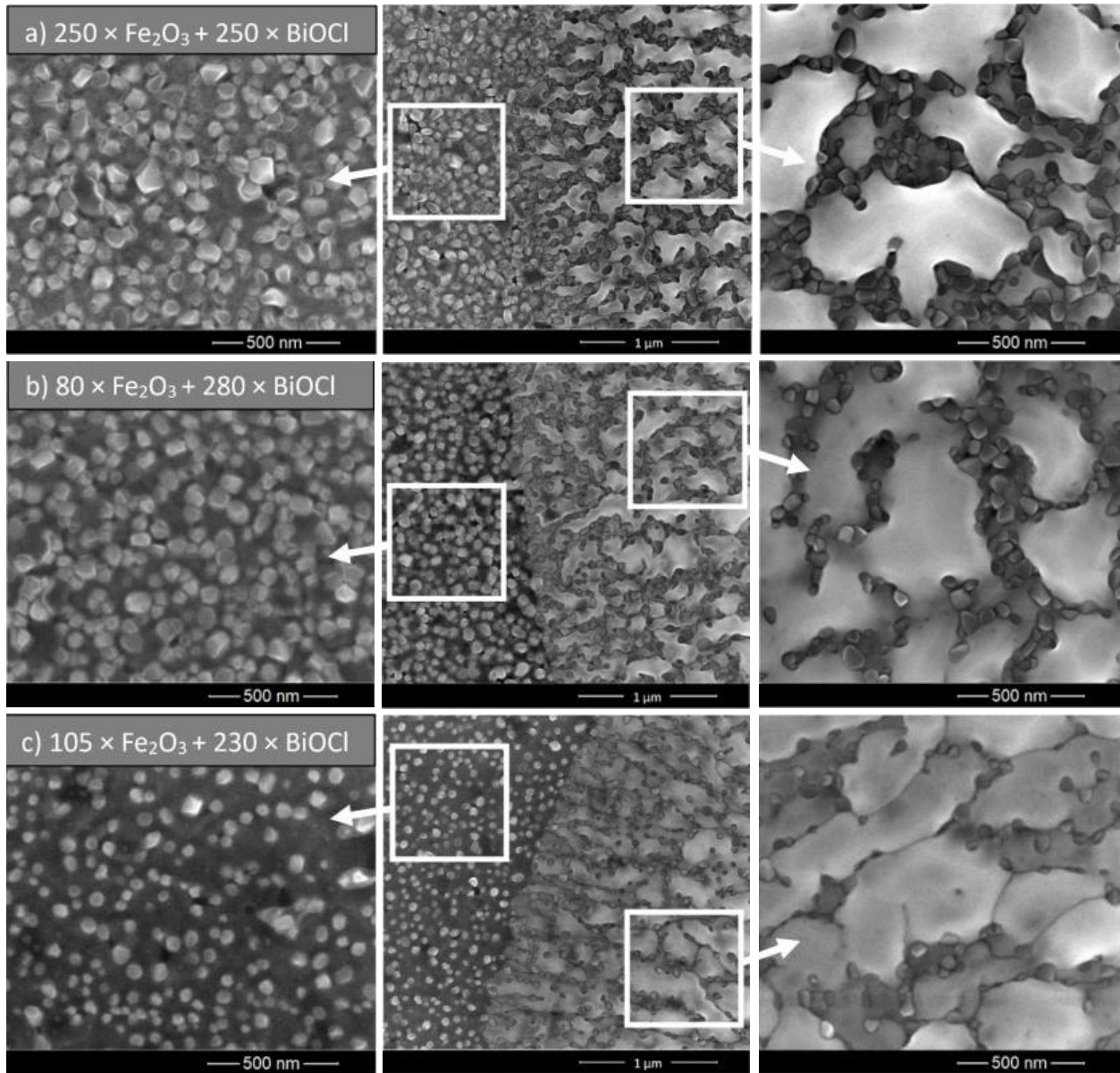

Figure 8: The bird-eye view of the SEM images of the a) Fe_2O_3 reference sample, b) BiOCl reference sample after annealing at 800 °C for 30 minutes.

Out of all annealed composites, three annealed two-component samples exhibited areas covered with grain-like features (Figure 9, left panels) neighboring with flat lighter plateau-like areas

(Figure 9, right panels) with distinctive boundaries between them (Figure 9, middle column). The concentration of the grain-like features, as estimated visually, increased with the increasing Fe_2O_3 layer thickness, and are thus to be related to the structural effect of Fe_2O_3. This statement is supported by the observation that the sample with the thinnest Fe_2O_3 layer of those visualized in Figure 9, i.e. the one grown using the cycle sequence of $105 \times Fe_2O_3 + 230 \times BiOCl$, exhibited larger voids between the grains.

The EDX analysis revealed that the flat plateau-like areas (Figure 9 right columns) contained several times more bismuth compared to the darker grainy areas (Figure 9 left columns), in addition to oxygen, carbon, and iron (See the Supplementary Material). This indicates that the flake-like features, i.e. BiOCl crystallites, were probably mainly transformed into these plateau-like smoother features by annealing process. An annealed sample grown using the cycle sequence of $175 \times Fe_2O_3 + 280 \times BiOCl$ differed from the other composites in terms of the morphology, demonstrating three different types of areas (See the Supplementary Material).

Figure 9: The bird-eye view of the SEM images of the a) $250 \times Fe_2O_3 + 250 \times BiOCl$, b) $80 \times Fe_2O_3 + 280 \times BiOCl$ and c) $105 \times Fe_2O_3 + 230 \times BiOCl$ structures after annealing at 800 °C for 30 minutes. On the middle panel, the transitions from the grainy areas to the round shaped areas are displayed. White boxes indicate the approximate areas where the higher magnification images indicated with arrows were taken from.

3.2 Magnetic and electrical behavior

In-plane magnetic measurements were performed for the selected as-deposited and annealed reference samples and composites. The hysteresis curves for the as-deposited state at room temperature displayed nonlinear and saturative magnetization and well-defined coercive fields in

the case of the majority of samples, demonstrating typical ferro- or ferrimagnetic behavior (Figure 10). One could notice that there is a deformation of the hysteresis loop of Fe_2O_3 reference sample at crossing the zero field (Figure 10.a), which may be connected to exchange bias and/or magnetic proximity effects [49, 50]. The three highest saturation magnetization values were 104 emu/cm^3, 60 emu/cm^3 and 29 emu/cm^3, measured at the external field values of 28 kOe, 35 kOe and 30 kOe for the sample grown using the cycle sequence of $105 \times Fe_2O_3 + 230 \times BiOCl$, Fe_2O_3 reference sample, and the sample grown using the cycle sequence of $175 \times Fe_2O_3 + 280 \times BiOCl$, respectively. This is in a good agreement with another study on ALD [4], where ε-Fe_2O_3 magnetization saturated almost fully at 50 kOe reaching a value of 96 emu/cm^3 at room temperature.

In our study, Fe_2O_3 reference sample (Figure 10.a) and the composite grown using the cycle sequence of $175 \times Fe_2O_3 + 280 \times BiOCl$ (Figure 10.b) possessed the highest coercive field (H_C) of 9757 Oe (776.4 kA/m) for both samples (Figure 10, inset figure). In the former study on ε-Fe_2O_3 [4], the H_C at 300 K was ~1.6 kOe. This is higher compared to that in our samples, but the difference in coercivity can at least partially be related to the different sample thicknesses and crystallite sizes.

Further, out of all as-grown two-component structures examined in our study, the sample grown using the cycle sequence of $175 \times Fe_2O_3 + 280 \times BiOCl$ (Figure 10.b) demonstrated, magnetically, the most well defined behavior compared to the other composites. As was determined by GIXRD, the latter was also the film showing higher peak intensities (especially the peaks connected to the ε-Fe_2O_3 phase) and was, therefore, crystallographically more ordered compared to the other composites. Magnetic properties can be directly influenced by the phase composition, and ordering in the layers can also enhance the magnetization. Furthermore, ε-Fe_2O_3 is known for its room-temperature multiferroic properties, including high coercivity [4, 6, 7]. At the same time, BiOCl is hardly recognized as magnetic material. In our reference BiOCl film, the thickness was only 7.8 nm and even somewhat decreased annealing. Since the measured magnetic moment was divided with total volume of the thin film, the noticeable saturation magnetization value in the case of reference BiOCl could be amplified by the noticeably smaller volume compared to the other samples, and should be treated with some caution.
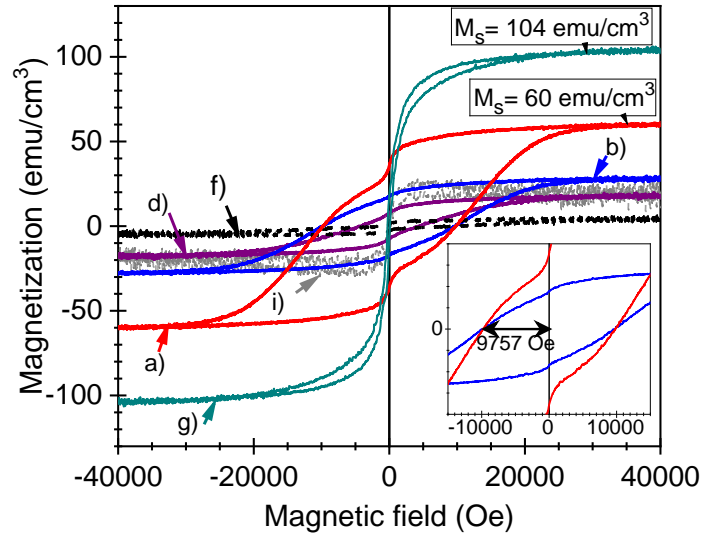
Figure 10: Magnetization vs. external magnetic field (**M-H**) curves at 300 K for the as-deposited selected samples. Substrate diamagnetism has been subtracted from the data. See Table I as the reference for the growth cycle sequences behind these diffractogram labels. The inset figure shows H_C values in the case of Fe_2O_3 reference sample (red) and sample grown using the cycle sequence of $175 \times Fe_2O_3 + 280 \times BiOCl$ (blue). M_s indicates saturation magnetization value.

Annealing noticeably reduced the magnetic behavior of the samples (Figure 11). The sample deposited using the sequence of $80 \times Fe_2O_3 + 280 \times BiOCl$ (Figure 11.d) had the highest saturation magnetization and coercivity values after annealing compared to other annealed samples. 175 emu/cm^3 and 35 Oe, respectively. This saturation magnetization value was higher than in the case of the as-deposited samples, but the coercivity remained several times lower. Plausibly, the change in magnetic behavior was caused by the Fe_2O_3 phase change from orthorhombic ε-Fe_2O_3 to rhombohedral α-Fe_2O_3 that took place during the annealing. Hematite, in general, is a well-known soft magnetic material, and in an earlier study of α-Fe_2O_3 thin films, weak ferromagnetic behavior at room temperature was also noted [51]
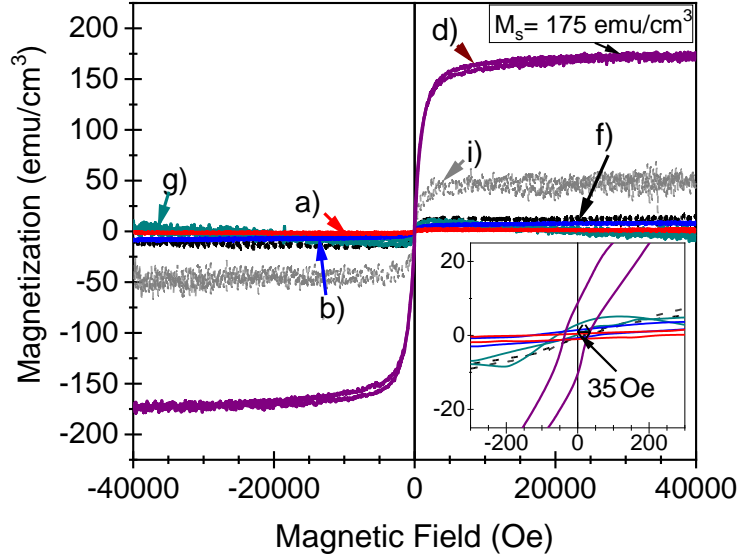
Figure 11: Magnetization vs. external magnetic field curves at 300 K for the selected samples after annealing at 800 °C for 30 minutes. Substrate diamagnetism has been subtracted from the data. See Table II as the reference for the growth cycle sequences behind these diffractogram labels. The inset figure shows H_C of the sample deposited using the sequence of $80 \times Fe_2O_3 + 280 \times BiOCl$ (purple). M_s indicates saturation magnetization value.

Electrical measurements revealed that the two dielectric layers in the as-deposited state were moderately leaky, and showed a semiconductor behavior. Consequently, a Schottky diode was formed at the junction in between each insulating film and the corresponding metal electrode. Therefore, the entire device can be seen as two diodes in opposition. Structures showed a rectifier like behavior and samples were affected by visible illumination as the current increased around 0.7 mA under illumination and this increase was independent of the negative applied bias (Figure 12 and 13, left panels). It is important to mention that light was not introduced through the metal covering the individual device, but through the surrounding area, which is not covered by the metal electrode. From the point of view of possible applications, at reverse bias the device acts like a photovoltaic cell. This can be related to the moderate bandgaps of the constituent compounds that also can be affected by modifications in structure and composition. The bandgap of BiOCl can depend on mechanical strains affecting the crystallite structure and vary between 2.33 and 3.34 eV [52]. The band-gap of BiOCl can also depend on its stoichiometry, and the band-gap for oxygen vacancy rich BiOCl has been reported as 3.12 eV [34]. At the same time, the band-gap of hematite Fe_2O_3 is 2.14-2.20 eV [53], and for ε-Fe_2O_3, it may decrease down to 1.6 eV [30]. The samples

23

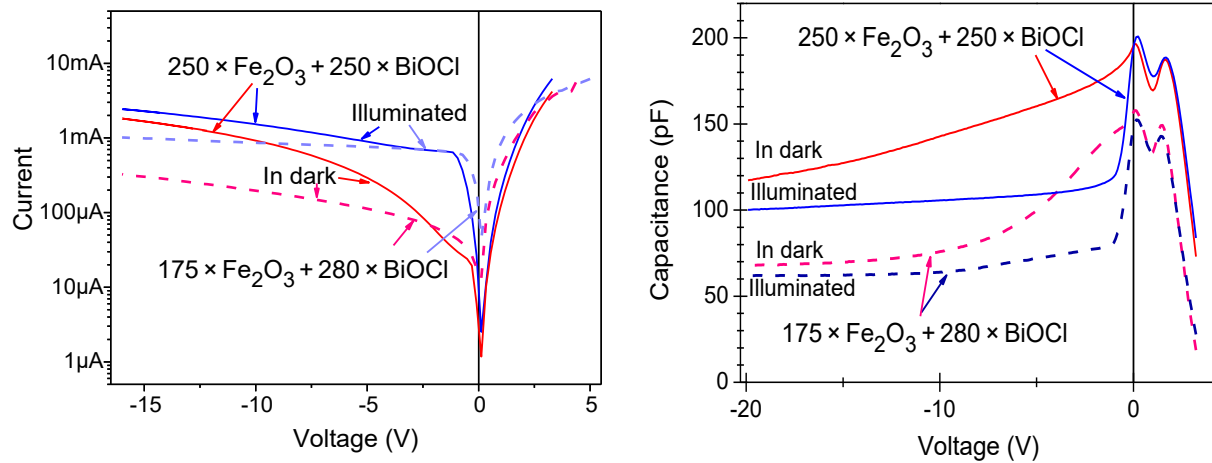deposited using the sequence of $80 \times Fe_2O_3 + 280 \times BiOCl$ (Figure 12, left panel) and $20 \times Fe_2O_3 + 250 \times BiOCl$ (not shown), i.e. the samples with the lowest number of Fe_2O_3 layers deposited, were more conductive at negative bias as tunneling currents through Fe_2O_3 dominates over the rectifying behavior. The influence of illumination was either not observed or much lower compared to the other samples.

Impedance measurements showed that in the case of the samples deposited using the sequences of $105 \times Fe_2O_3 + 230 \times BiOCl$ and $80 \times Fe_2O_3 + 280 \times BiOCl$, capacitance increased with negative voltage (Figure 12, right panel). This behavior suggests that the interface between BiOCl and Fe_2O_3 acts as an energy barrier for electrons. When negative voltage is applied, electrons remain confined at the BiOCl layer, which in result is highly electron-populated. Consequently, the Fe_2O_3 film layer behaved as an effectively insulating layer compared to BiOCl and, therefore, the capacitance increased. On the other hand, in the case of the samples with higher thicknesses, deposited using the sequences of $250 \times Fe_2O_3 + 250 \times BiOCl$ and $175 \times Fe_2O_3 + 280 \times BiOCl$, the C-V curves differed noticeably (Figure 13, right panel). Capacitance was maximum at zero bias, decreased with voltage regardless the voltage sign, and was affected by the illumination. As the Fe_2O_3 film thickness increases, it becomes less conductive and the device behaves as two opposite diodes. Therefore, the capacitance is mainly due to the reversely biased junction and decreases with voltage.
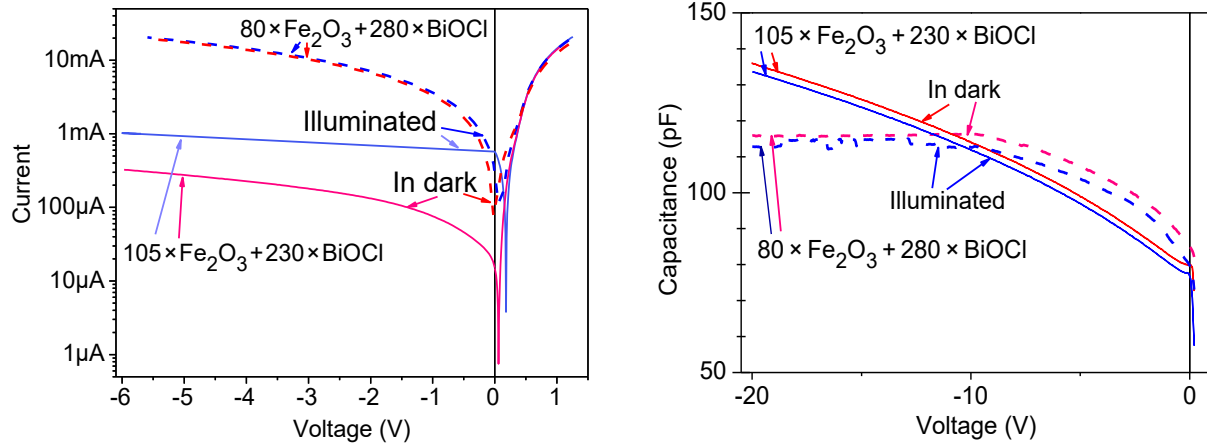
Figure 12: Current versus voltage curves (left panel) and capacitance versus voltage (C-V) curves (right panel) for the samples deposited using the sequences of $105 \times Fe_2O_3 + 230 \times BiOCl$ and $80 \times Fe_2O_3 + 280 \times BiOCl$ measured in the darkness and under illumination. Bottom electrode was Al\Si\TiN and top electrode was Ti/Al for both samples.

Figure 13: Current versus voltage curves (left panel) and capacitance versus voltage (C-V) curves (right panel) for the samples deposited using the sequences of $250 \times Fe_2O_3 + 250 \times BiOCl$ and $175 \times Fe_2O_3 + 280 \times BiOCl$ measured in the darkness and under illumination. Bottom electrode was Al\Si\TiN and top electrode was Ti/Al for both samples.

4. Conclusion

Two-component crystalline thin film structures consisting of orthorhombic ε-Fe₂O₃ layer at the bottom and tetragonal BiOCl nanoflakes on the top were successfully grown using atomic layer deposition. Surface morphology studies revealed that grain-like and flake-like features were formed on smooth surface, related to the growth of separate ε-Fe₂O₃ and BiOCl crystals, respectively. BiOCl layer could not be formed as dense continuous film on ε-Fe₂O₃ layer. This noticeably uneven surface may possibly limit the applications of such composites. Studies on three dimensional, trenched, structures confirmed that the ε-Fe₂O₃ thin film can be deposited also to the inner regions of the 3D structures, which might be regarded as a pre-requisite before possible applications in semiconductor industry and memory devices. The structures in the as-deposited state demonstrated ferromagnetic-like behavior at room temperature. The magnetization was nonlinear, saturative and hysteretic with well-defined coercive fields in the majority of samples. The strongest coercive fields were determined in the samples where the ε-Fe₂O₃ phase dominated and the highest H_C value was 9.7 kOe. Electrical measurements revealed that the deposited structures were moderately leaky, possibly due to uneven surface of the composites. The structures

demonstrated rectifier type behavior and the conduction currents in the samples were affected by visible light illumination as the current increased around 0.7 mA under illumination. Annealing changed the surface morphology, with phase composition transformed from orthorhombic ε-Fe_2O_3 with tetragonal BiOCl to rhombohedral α-Fe_2O_3 with cubic and monoclinic Bi_2O_3 polymorphs. The annealing also reduced the magnetic performance of the samples. In future, photosensitivity of Fe_2O_3/BiOCl heterojunctions might potentially become tailored with magnetization of Fe_2O_3, in nanocomposites, thus creating novel light-sensitive magnetic materials.

5. Acknowledgements

References

[1] K. Yamamoto, T. Matsuda, K. Nishibayashi, Y. Kitamoto, H. Munekata, Low-power photo-induced precession of magnetization in ultra-thin Co/Pd multilayer films, IEEE Trans. Magn. 49 (2013) 3155–3158. https://doi.org/10.1109/TMAG.2013.2240379.

[2] M. Li, Y. Wang, A. Chen, A. Naidu, B. S. Napier, W. Li, C. L. Rodriguez, S. A. Crooker, F. G. Omenetto, Flexible magnetic composites for light-controlled actuation and interfaces. Proc. Natl. Acad. Sci. 115 (2018) 8119–8124. https://doi.org/10.1073/pnas.1805832115.

[3] A. I. Kuznetsov, A. E. Miroshnichenko, Y. H. Fu, J. Zhang, & B. Luk'yanchuk, Magnetic light. Sci. Rep. 2 (2012) 1–6. https://doi.org/10.1038/srep00492.

[4] A. Tanskanen, O. Mustonen, M. Karppinen, Simple ALD process for ε-Fe_2O_3 thin films, APL Mater. 5 (2017) 056104. https://doi.org/10.1063/1.4983038.

[5] M. Yoshikiyo, K. Yamada, A. Namai, S. Ohkoshi, Study of the electronic structure and magnetic properties of ε-Fe_2O_3 by first-principles calculation and molecular orbital calculations, J. Phys. Chem. C 116 (2012) 8688–8691. https://doi.org/10.1021/jp300769z.

[6] M. Gich, I. Fina, A. Morelli, F. Sánchez, M. Alexe, J. Gàzquez, J. Fontcuberta, A. Roig, Multiferroic Iron Oxide Thin Films at Room Temperature, Advanced Materials 26 (2014) 4645–4652. https://doi.org/10.1002/adma.201400990.

[7] J. Jin, S. Ohkoshi, K. Hashimoto, Giant coercive field of nanometer- sized iron oxide, Adv. Mater. 16 (2004) 48–51. https://doi.org/10.1002/adma.200305297.

[8] M. Gich, C. Frontera, A. Roig, J. Fontcuberta, E Molins, N. Bellido, C. Simon, C. Fleta, Magnetoelectric coupling in ε-Fe$_2$O$_3$ nanoparticles, Nanotechnology 17 (2006) 687–691. https://doi.org/10.1088/0957-4484/17/3/012.

[9] Volume A: Space-Group Symmetry, in: T. Hahn (Ed.), International Tables for Crystallography, Kluwer Academic, London, 1992, pp 786–789.

[10] H. Peng, C. K. Chan, S. Meister, X. F. Zhang, Y. Cui, Shape evolution of layer-structured bismuth oxychloride nanostructures via low-temperature chemical vapor transport, Chem. Mater. 21 (2009) 247–252. https://doi.org/10.1021/cm802041g.

[11] X. Liu, C. Fan, Y. Wang, Y. Wang, X. Zhang, Z. Liang, Sci. Low temperature preparation of flower-like BiOCl film and its photocatalytic activity, China Chem. 55 (2012) 2438–2444. https://doi.org/10.1007/s11426-012-4549-2.

[12] X. Zhang, R. Li, Y. Wang, X. Zhang, Y. Wang, C. Fan, Slow-releasing Cl- to prepare BiOCl thin film on Bi plate and its photocatalytic properties, Mater. Lett. 174 (2016) 126–128. https://doi.org/10.1016/j.matlet.2016.03.109.

[13] E. L. Cuellar, J. O. Cortéz, A. M. Cruz, A. G. Loera, U. O. Méndez, Photocatalytic activity of BiOCl thin films deposited by thermal evaporation, Thin Solid Films 659 (2018) 57–63. https://doi.org/10.1016/j.tsf.2018.04.044.

[14] G. K. Tripathi, K. K. Saini, R. Kurchania, Synthesis of nanoplate bismuth oxychloride—a visible light active material, Opt. Spectrosc. 119 (2015) 656–663. https://doi.org/10.1134/S0030400X15100136.

[15] A. A. Dakhel, Hydrogen influenced the structural and optical properties of Ni-doped BiOCl nanocomposite: creation of FM properties, Appl. Phys. A 125 (2019) 89. https://doi.org/10.1007/s00339-019-2393-3.

[16] L. Xu, P. Yan, H. Li, S. Ling, J. Xia, J. Qiu, Q. Xu, H. Li, S. Yuan, Metallic Bi self-doping BiOCl composites: Synthesis and enhanced photoelectrochemical performance, Mater. Lett. 196 (2017) 225–229. https://doi.org/10.1016/j.matlet.2017.03.008.

[17] C.-Y. Wang, Y.-J. Zhang, W.-K. Wang, D.-N. Pei, G.-X. Huang, J.-J. Chen, X. Zhang, H.-Q. Yu, Enhanced photocatalytic degradation of bisphenol A by Co-doped BiOCl nanosheets under visible light irradiation, Appl. Catal. B Environ. 221 (2018) 320–328. https://doi.org/10.1016/j.apcatb.2017.09.036.

[18] M. Gao, D. Zhang, X. Pu, H. Li, W. Li, X. Shao, D. Lv, B. Zhang, J. Dou, Combustion synthesis of Fe-doped BiOCl with high visible-light photocatalytic activities, Sep. Purif. Technol. 162 (2016) 114–119. https://doi.org/10.1016/j.seppur.2016.02.024.

[19] K. Micheal, A. Ayeshamariam, R. Boddula, P. Arunachalam, M. S. AlSalhi, J. Theerthagiri, S. Prasad, J. Madhavan, A. M. Al-Mayouf, Assembled composite of hematite iron oxide on sponge-like BiOCl with enhanced photocatalytic activity, Mater. Sci. Energy Technol. 2 (2019) 104–111. https://doi.org/10.1016/j.mset.2018.11.004.

[20] L. Zhang, W. Wang, L. Zhou, M. Shang, S. Sun, Fe_3O_4 coupled BiOCl: A highly efficient magnetic photocatalyst, Appl. Catal. B Environ. 90 (2009) 458–462. https://doi.org/10.1016/j.apcatb.2009.04.005.

[21] K. Li, Y. Liang, J. Yang, H. Zhang, G. Yang, W. Lei, BiOCl/Fe2O3 heterojunction nanoplates with enhanced visible-light-driven photocatalytic performance for degrading organic pollutants and reducing Cr(VI), J. Photochem. Photobiol. Chem. 364 (2018) 240–249. https://doi.org/10.1016/j.jphotochem.2018.06.001.

[22] Y. Zheng, X. Zhang, J. Zhao, P. Yang, Assembled fabrication of α-Fe_2O_3/BiOCl heterojunctions with enhanced photocatalytic performance, Appl. Surf. Sci. 430 (2018) 585–594. https://doi.org/10.1016/j.apsusc.2017.06.097.

[23] N. Li, Y. Jin, X. Hua, K. Wang, J. Xu, M. Chen, F. Teng, Uniform Fe_2O_3 nanocubes on BiOCl nanosheets and its improved photocatalytic activity, J. Mol. Catal. Chem. 395 (2014) 428–433. https://doi.org/10.1016/j.molcata.2014.08.045.

[24] N. Li, X. Hua, K. Wang, Y. Jin, J. Xu, M. Chena, F. Teng, In situ synthesis of uniform Fe_2O_3/BiOCl p/n heterojunctions and improved photodegradation properties for mixture dyes, Dalton Trans. 43 (2014) 13742–13750. https://doi.org/10.1039/C4DT01999G.

[25] M. Gich, J. Gazquez, A. Roig, A. Crespi, J. Fontcuberta, J. C. Idrobo, S. J. Pennycook, M. Varela, V. Skumryev, M. Varela, Epitaxial stabilization of ε-Fe_2O_3 (00l) thin films on $SrTiO_3$ (111), Appl. Phys. Lett. 96 (2010) 112508. https://doi.org/10.1063/1.3360217.

[26] S. S. Kulkarni, C. D. Lokhande, Structural, optical, electrical and dielectrical properties of electrosynthesized nanocrystalline iron oxide thin films, Mater. Chem. Phys. 82 (2003) 151–156. https://doi.org/10.1016/S0254-0584(03)00212-8.

[27] J. Tuček, R. Zbořil, A. Namai, S. Ohkoshi, ε-Fe$_2$O$_3$: An advanced nanomaterial exhibiting giant coercive field, millimeter-wave ferromagnetic resonance, and magnetoelectric coupling, Chem. Mater. 22 (2010) 6483–6505. https://doi.org/10.1021/cm101967h.

[28] V. N. Nikolić, M. Tadić, M. Panjan, L. Kopanja, N. Cvjetićanin, V. Spasojević, Influence of annealing treatment on magnetic properties of Fe$_2$O$_3$/SiO$_2$ and formation of ε-Fe$_2$O$_3$ phase, Ceram. Int. 43 (2017) 3147–3155. https://doi.org/10.1016/j.ceramint.2016.11.132.

[29] J. López-Sánchez, A. Serrano, A. Del Campo, M. Abuín, O. Rodríguez de la Fuente, N. Carmona, Sol–gel synthesis and micro-raman characterization of ε-Fe$_2$O$_3$ micro- and nanoparticles, Chem. Mater. 28 (2016) 511–518. https://doi.org/10.1021/acs.chemmater.5b03566.

[30] B. David, N. Pizúrová, P. Synek, V. Kudrle, O. Jašek, O. Schneeweiss, ε-Fe$_2$O$_3$ nanoparticles synthesized in atmospheric-pressure microwave torch, Mater. Lett., 116 (2014) 370–373. https://doi.org/10.1016/j.matlet.2013.11.057.

[31] D. Barreca, G. Carraro, D. Peeters, A. Gasparotto, C. Maccato, W. M. M. Kessels, V. Longo, F. Rossi, E. Bontempi, C. Sada, A. Devi, Surface decoration of ε-Fe$_2$O$_3$ nanorods by CuO via a two-step CVD/sputtering approach**, Chem. Vap. Depos. 20 (2014) 313–319. https://doi.org/10.1002/cvde.201407108.

[32] V. Miikkulainen, M. Leskelä, M. Ritala, R. L. Puurunen, Crystallinity of inorganic films grown by atomic layer deposition: Overview and general trends, J. Appl. Phys. 113 (2013) 021301. https://doi.org/10.1063/1.4757907.

[33] H. Kim, H.-B.-R. Lee, W.-J. Maeng, Applications of atomic layer deposition to nanofabrication and emerging nanodevices, Thin Solid Films 517 (2009) 2563–2580. https://doi.org/10.1016/j.tsf.2008.09.007.

[34] D. Cui, L. Wang, K. Xu, L. Ren, L. Wang, Y. Yu, Y. Du, W. Hao, Band-gap engineering of BiOCl with oxygen vacancies for efficient photooxidation properties under visible-light irradiation, J. Mater. Chem. A 6 (2018) 2193–2199. https://doi.org/10.1039/C7TA09897A.

[35] J.-M. Song, C.-J. Mao, H.-L. Niu, Y.-H. Shen, S.-Y. Zhang, Hierarchical structured bismuth oxychlorides: self-assembly from nanoplates to nanoflowers via a solvothermal route and their

photocatalytic properties, CrystEngComm 12 (2010) 3875–3881. https://doi.org/10.1039/C003497P

[36] Z. S. Seddigi, M. A. Gondal, U. Baig, S. A. Ahmed, M. A. Abdulaziz, E. Y. Danish, M. M. Khaled, A. Lais, Facile synthesis of light harvesting semiconductor bismuth oxychloride nano photo-catalysts for efficient removal of hazardous organic pollutants, PLOS ONE 12 (2017) e0172218. https://doi.org/10.1371/journal.pone.0172218.

[37] D. S. Bhachu, S. J. A. Moniz, S. Sathasivam, D. O. Scanlon, A. S. Walsh, M. Bawaked, M. Mokhtar, A. Y. Obaid, I. P. Parkin, J. Tang, C. J. Carmalt, Bismuth oxyhalides: synthesis, structure and photoelectrochemical activity, Chem. Sci. 7 (2016) 4832-4841. https://doi.org/10.1039/C6SC00389C.

[38] I. D. Sharma, G. K. Tripathi, V. K. Sharma, S. N. Tripathi, R. Kurchania, C. Kant, A. K. Sharma, K. K. Saini, One-pot synthesis of three bismuth oxyhalides (BiOCl, BiOBr, BiOI) and their photocatalytic properties in three different exposure conditions, Cogent Chem. 1 (2015) 1076371. https://doi.org/10.1080/23312009.2015.1076371.

[39] M. Vehkamäki, T. Hatanpää, M. Ritala, M. Leskelä, Bismuth precursors for atomic layer deposition of bismuth-containing oxide films, J. Mater. Chem. 14 (2004) 3191–3197. https://doi.org/10.1039/B405891G.

[40] M. Schuisky, CVD and ALD in the Bi-Ti-O System. In Acta Univ. Ups. Comprehensive Summaries of Uppsala Dissertations from the Faculty of Science and Technology 594; Eklundshof Grafiska AB, Uppsala, 2000, pp 1-47.

[41] T. Arroval, L. Aarik, R. Rammula, V. Kruusla, J. Aarik, Effect of substrate-enhanced and inhibited growth on atomic layer deposition and properties of aluminum–titanium oxide films, Thin Solid Films 600 (2016) 119–125. https://doi.org/10.1016/j.tsf.2016.01.024.

[42] K. J. Hughes, J. R. Engstrom, Nucleation delay in atomic layer deposition on a thin organic layer and the role of reaction thermochemistry, J. Vac. Sci. Technol. A 30 (2012) 01A102. https://doi.org/10.1116/1.3625564.

[43] S. S. Lee, J. Y. Baik, K.-S. An, Y. D. Suh, J.-H. Oh, Y. Kim, Reduction of incubation period by employing OH-terminated Si(001) substrates in the atomic layer deposition of Al_2O_3, J. Phys. Chem. B 108 (2004) 15128-15132. https://doi.org/10.1021/jp048038b.

[44] C. E. Nanayakkara, A. Vega, G. Liu, C. L. Dezelah, R. K Kanjolia, Y. J. Chabal, Role of initial precursor chemisorption on incubation delay for molybdenum oxide atomic layer deposition, Chem. Mater. 28 (2016) 8591-8597. https://doi.org/10.1021/acs.chemmater.6b03423.

[45] S. Ohkoshi, S. Sakurai, J. Jin, K. Hashimoto, The addition effects of alkaline earth ions in the chemical synthesis of ε-Fe_2O_3 nanocrystals that exhibit a huge coercive field, J. Appl. Phys. 97 (2005), 10K312. https://doi.org/10.1063/1.1855615.

[46] R. Zboril, M. Mashlan, K. Barcova, M. Vujtek, Thermally induced solid-state syntheses of γ-Fe_2O_3 nanoparticles and their transformation to α-Fe_2O_3 via ε-Fe_2O_3, Hyperfine Interact. 139 (2002) 597–606. https://doi.org/10.1007/978-94-010-0299-8_65.

[47] E. Tronc, C. Chanéac, J. P. Jolivet, Structural and magnetic characterization of ε-Fe_2O_3, J. Solid State Chem. 139 (1998) 93–104. https://doi.org/10.1006/jssc.1998.7817.

[48] Y. R. Yao, W. Z. Huang, H. Zhou, Y. F. Zheng, X. C. Song, Self-assembly of dandelion-like Fe_3O_4@C@BiOCl magnetic nanocomposites with excellent solar-driven photocatalytic properties, J. Nanoparticle Res. 16 (2014) 2451. https://doi.org/10.1007/s11051-014-2451-x.

[49] P. K. Manna, S. M. Yusuf, Two interface effects: Exchange bias and magnetic proximity, Phys. Rep. 535 (2014) 61–99. https://doi.org/10.1016/j.physrep.2013.10.002.

[50] J. Y. Chen, N. Thiyagarajah, H. J. Xu, J. M. D. Coey, Perpendicular exchange bias effect in sputter-deposited CoFe/IrMn bilayers, Appl. Phys. Lett. 104 (2014) 152405. https://doi.org/10.1063/1.4871711.

[51] F. F. H. Aragón, J. D. Ardisson, J. C. R. Aquino, I. Gonzalez, W. A. A. Macedo, J. A. H. Coaquira, J. Mantilla, S. W. Silva, P. C. Morais, Effect of the thickness reduction on the structural, surface and magnetic properties of α-Fe_2O_3 thin films, Thin Solid Films 607 (2016) 50–54. https://doi.org/10.1016/j.tsf.2016.03.052.

[52] L. Zhang, Z. K. Tang, W. M. Lau, W. J. Yin, S. X. Hu, L. M. Liu, Tuning band gaps and optical absorption of BiOCl through doping and strain: insight form DFT calculations, Phys. Chem. Chem. Phys. 19 (2017) 20968–20973. https://doi.org/10.1039/C7CP03276E.

[53] S. Piccinin, The band structure and optical absorption of hematite (α-Fe_2O_3): a first-principles GW-BSE study, Phys. Chem. Chem. Phys. 21 (2019) 2957–2967. https://doi.org/10.1039/C8CP07132B.